



# Wave Generation by Flare-accelerated Ions and Implications for $^3\text{He}$ Acceleration

A. Fitzmaurice<sup>1,2</sup>, J. F. Drake<sup>2,3</sup> , and M. Swisdak<sup>1,2</sup> <sup>1</sup> Department of Physics, University of Maryland, College Park, MD 20740, USA<sup>2</sup> Institute for Research in Electronics and Applied Physics, University of Maryland, College Park, MD 20740, USA<sup>3</sup> Department of Physics, the Institute for Physical Science and Technology and the Joint Space Institute, University of Maryland, College Park, MD 20740, USA

Received 2023 November 17; revised 2024 January 17; accepted 2024 January 21; published 2024 March 20

## Abstract

The waves generated by high-energy proton and alpha particles streaming from solar flares into regions of colder plasma are explored using particle-in-cell simulations. Initial distribution functions for the protons and alphas consist of two populations: an energetic, streaming population represented by an anisotropic ( $T_{\parallel} > T_{\perp}$ ), one-sided kappa function and a cold, Maxwellian background population. The anisotropies and nonzero heat fluxes of these distributions destabilize oblique waves with a range of frequencies below the proton cyclotron frequency. These waves scatter particles out of the tails of the initial distributions along constant-energy surfaces in the wave frame. Overlap of the nonlinear resonance widths allows particles to scatter into near-isotropic distributions by the end of the simulations. The dynamics of  $^3\text{He}$  are explored using test particles. Their temperatures can increase by a factor of nearly 20. Propagation of such waves into regions above and below the flare site can lead to heating and transport of  $^3\text{He}$  into the flare acceleration region. The amount of heated  $^3\text{He}$  that will be driven into the flare site is proportional to the wave energy. Using values from our simulations, we show that the abundance of  $^3\text{He}$  driven into the acceleration region should approach that of  $^4\text{He}$  in the corona. Therefore, waves driven by energetic ions produced in flares are a strong candidate to drive the enhancements of  $^3\text{He}$  observed in impulsive flares.

*Unified Astronomy Thesaurus concepts:* Solar energetic particles (1491); Solar physics (1476); Solar flares (1496); Space plasmas (1544)

## 1. Introduction

Solar energetic particles (SEPs) accelerated in impulsive flares provide essential clues to the flare energy release process. Due to the lack of in situ coronal data, observations of these events are made through remote sensing of radio, X-ray, gamma-ray, and extreme ultraviolet emissions. While this has led to progress in understanding the acceleration and scattering of energetic electrons in impulsive flares, information on the ion dynamics from remote-sensing data is limited to flares with significant gamma-ray emission, which typically only involve particles with energies in the MeV range and are rarely associated with impulsive SEPs (Shih et al. 2009; Lin 2011). As a result, in situ measurements of the spectra of energetic ions in the solar wind have been essential in exploring flare-driven ion acceleration (Reames 1999; Mason 2007; Bučík 2020; Reames 2021).

A characteristic feature of impulsive events is the strong enhancement of the  $^3\text{He}/^4\text{He}$  abundance ratio at high energies, which in some cases is a factor of  $10^4$  greater than the typical ratios observed in the quiet-time corona and solar wind (Reames 1999; Mason 2007). This preferential acceleration of  $^3\text{He}$  is assumed to be associated with cyclotron resonance interactions due to the unique charge-to-mass ratio of this species, an idea first proposed by Fisk (1978). The cyclotron frequency of fully stripped  $^3\text{He}$  (two-thirds of the proton cyclotron frequency) is distinct from that of other ions in the coronal environment. As a result, waves generated near its cyclotron frequency will be preferentially absorbed by  $^3\text{He}$ , while waves around the  $^4\text{He}$  cyclotron frequency may be

absorbed by other ion species, thus raising the  $^3\text{He}/^4\text{He}$  ratio at high temperatures.

Fisk (1978) proposed a two-stage mechanism whereby electron–ion drifts produced during reconnection excite electrostatic ion cyclotron waves that preferentially heat  $^3\text{He}$  through its cyclotron resonance. A secondary process with some minimum threshold velocity would then accelerate the  $^3\text{He}$  to observed energies. Unfortunately, to produce waves of the correct frequency range, Fisk (1978) requires at least 20%  $^4\text{He}$  number density, an abundance much higher than what is typically observed in the corona (Gabriel et al. 1995; Moses et al. 2020).

Temerin & Roth (1992) and Roth & Temerin (1997) propose a different mechanism which does not require such a high  $^4\text{He}$  abundance. They suggest reconnection-driven electron jets produce oblique electromagnetic cyclotron waves at frequencies just below the proton cyclotron frequency. As these waves propagate into regions of stronger magnetic field in the lower corona, their frequency remains constant while the local cyclotron frequencies of the coronal ion species increase. Since  $^3\text{He}$  has the next highest cyclotron frequency after hydrogen, it will resonate with these waves first, and therefore preferential acceleration can occur. Additional heating of partially stripped heavy ions could also occur due to resonances at the second or higher harmonics. This model has recently been used to explain simultaneous  $^3\text{He}$  and ultra-heavy ion enhancements observed by Solar Orbiter (Mason et al. 2023). However, while there is evidence from terrestrial observations that cyclotron waves are generated by auroral electrons, the growth rates for this instability are small for coronal values of the electron beam energy and  $\omega_{pe}/\Omega_{pe}$  (Temerin & Lysak 1984). Thus, the source of the waves capable of accelerating  $^3\text{He}$  remains an open question.

Both of these proposed mechanisms, along with several others (e.g., Zhang 1999; Paesold et al. 2003), have assumed that flare-accelerated electrons are the source of free energy



Original content from this work may be used under the terms of the [Creative Commons Attribution 4.0 licence](https://creativecommons.org/licenses/by/4.0/). Any further distribution of this work must maintain attribution to the author(s) and the title of the work, journal citation and DOI.

driving the waves responsible for  $^3\text{He}$  acceleration. However, simulations show that ions gain more energy than electrons during magnetic reconnection (Eastwood et al. 2013) and recent observations from Parker Solar Probe have found waves in the proton cyclotron frequency band associated with ion beams in the solar wind (Verniero et al. 2020). We propose a mechanism for  $^3\text{He}$  acceleration that combines the ideas of Fisk (1978) and Temerin & Roth (1992) but takes flare-accelerated ions, rather than electrons, as the wave driver. To explore this hypothesis, we perform initial-value simulations to identify and analyze the effects of instabilities that form due to high-energy ion populations streaming away from flare sites. We begin with a brief review of linear ion instabilities and associated particle scattering in Section 2. In Section 3, we describe the simulation setup and parameters. Results of wave evolution, particle scattering, and  $^3\text{He}$  heating are presented in Section 4. Finally, we end with a discussion of the implications for  $^3\text{He}$  acceleration and a summary of conclusions in Section 5.

## 2. Background

### 2.1. Linear Ion Instabilities

Linear ion instabilities have previously been explored in studies of interplanetary shocks (Winske & Leroy 1984; Gary 1985; Wilson 2016) and the near-Earth solar wind (Gary et al. 1976). From this work, there are five instabilities which could be relevant for our simulations: the left-hand resonant, right-hand resonant, and nonresonant instabilities excited by ion beams streaming parallel to the magnetic field; and the parallel and oblique fire-hose instabilities associated with temperature anisotropies of the form  $T_{\parallel}/T_{\perp} > 1$ , where the subscripts denote direction with respect to the magnetic field.

For this discussion, an instability is considered resonant with a particle population if there are a sufficient number of particles with parallel velocities that satisfy the resonance condition:

$$\omega - k_{\parallel}v_r \pm n\Omega_{ci} = 0, \quad (1)$$

where  $\omega$  is the wave frequency,  $k_{\parallel}$  is the field-aligned component of the wavevector,  $\Omega_{ci}$  is the cyclotron frequency of the particle species, and the sign of the final term depends on the polarization of the wave (positive for right-handed waves and negative for left-handed waves). For parallel propagating waves, there is only the  $n=1$  resonance. In this case, the resonant velocity  $v_r$  corresponds to the frame where the Doppler-shifted frequency of the wave matches the cyclotron frequency of the particle. Particles with parallel velocities equal to the resonant velocity will experience a constant electric field and can coherently exchange energy with the wave. In the oblique case, there are an infinite number of resonances corresponding to integer multiples of the cyclotron frequency ( $n = 0, \pm 1, \pm 2, \dots$ ).

Gary et al. (1984), Gary (1991), and Gary (1993) provide an extensive review of the instabilities caused by counter-streaming ion populations. Assuming simplified velocity distributions, where both beam and core ions are represented by drifting Maxwellians, there are three modes which can be excited based on the beam temperature, density, and drift speed.

The right-hand circularly polarized mode, emerging from the magnetosonic branch of the dispersion relation, is the dominant mode for cool, tenuous beams with low-to-moderate drift

speeds. This mode propagates parallel to the magnetic field with a phase velocity  $v_p \approx v_A$  and frequencies  $\omega \lesssim \Omega_{ci}$ . As the temperature of the beam is increased, a left-hand circularly polarized mode from the Alfvén/ion cyclotron branch is also driven unstable. Like the right-hand mode, it propagates parallel to the magnetic field with  $v_p \approx v_A$  and  $\omega \lesssim \Omega_{ci}$ . Both modes are resonant with the beam ions, and thus we refer to them as the right-hand resonant and left-hand resonant instabilities. For cool, fast beams with considerable densities, the dominant mode is purely growing ( $\omega \approx 0$ ) and nonresonant for both the core and beam ion populations. We refer to this as the nonresonant instability.

In addition to ion beam instabilities, we also consider instabilities induced by the temperature anisotropy  $T_{\parallel}/T_{\perp} > 1$ . In the MHD limit, this produces the purely growing fire-hose instability with the threshold  $\beta_{\parallel} - \beta_{\perp} = 2$ . On kinetic scales, assuming a bi-Maxwellian distribution, this mode has frequencies  $\omega \lesssim \Omega_{ci}$  and it propagates parallel to the magnetic field with a phase velocity  $v_p \gtrsim v_A$  and a right-handed polarization (Kennel & Petschek 1966; Gary 1993). As shown in Gary et al. (1976), the threshold for instability is also slightly reduced in this regime. While the classic fire-hose instability emerges from the magnetosonic branch of the dispersion relation, Hellinger & Matsumoto (2000) found that the Alfvén branch can also be driven unstable by the same anisotropy, producing a purely growing and strongly oblique instability.

### 2.2. Resonance Widths and Quasi-linear Particle Diffusion

For parallel propagating waves, the electric field goes to zero in the reference frame moving with the wave. Therefore, wave-particle interactions in this frame conserve energy. For the nonrelativistic case we consider in this paper, this constrains resonant particle motion in  $v_{\parallel} - v_{\perp}$  phase space to concentric circles centered at the phase speed of the wave. How far particles are able to scatter along these surfaces depends on the nonlinear resonance widths, which were derived in Karimabadi et al. (1990) using formal Hamiltonian theory. For low-amplitude waves, marginal stability can be reached when the gradients along the resonant portions of the distribution function have been reduced to zero (Kennel & Engelmann 1966). However, in the case of oblique waves or multiple modes of varying wavenumbers and phase speeds, large amplitudes can result in significant resonance overlap, allowing for open phase-space orbits corresponding to arbitrarily high energies (Karimabadi et al. 1992). In this case, particles will be continuously heated until the waves are damped or until the wave amplitude has decreased to a point where the resonances no longer overlap.

## 3. Simulation Parameters

We perform fully kinetic, 2.5D simulations using the particle-in-cell (PIC) code p3d (Zeiler et al. 2002), in which we follow the self-consistent dynamics of three particle species: electrons, protons, and alpha particles. The number density of the alphas is 5% that of the protons, and additional electrons are added in order to balance the charge density. Due to the low abundance of  $^3\text{He}$  in the corona, we assume that this population has a negligible effect on the dynamics of the system and thus include it as a population of test particles.

We use normalized units in our simulations. All lengths are normalized to the proton inertial length  $d_p$ , all times to the inverse of the proton cyclotron frequency  $\Omega_{cp}^{-1}$ , all speeds to the

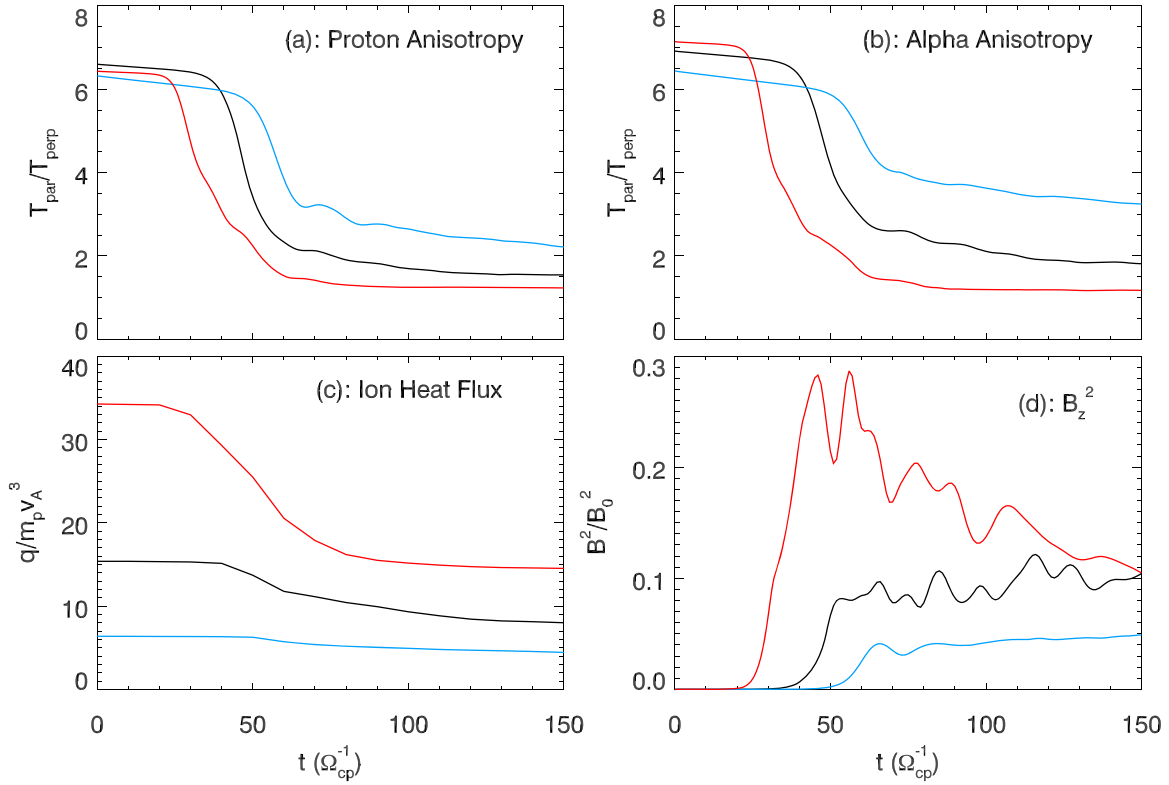


**Figure 1.** (a) Proton  $T_{\parallel}/T_{\perp}$ , (b) alpha  $T_{\parallel}/T_{\perp}$ , (c) combined proton and alpha heat flux, and (d) perpendicular magnetic energy vs. time for each case. Run 1 ( $T_{\kappa,x} = 10m_p v_A^2$ ) is plotted in black, Run 2 ( $T_{\kappa,x} = 5m_p v_A^2$ ) is plotted in blue, and Run 3 ( $T_{\kappa,x} = 20m_p v_A^2$ ) is plotted in red. The ion temperatures and perpendicular magnetic field data are output directly by the code every  $1 \Omega_{cp}^{-1}$ . The quantities shown here are the averages over the whole domain at each time. The heat fluxes are calculated using the 3D distribution functions and therefore data are only available every  $10 \Omega_{cp}^{-1}$ .

proton Alfvén speed  $v_A$ , and all temperatures to  $m_p v_A^2$ . In order to reduce the computational cost, we take the standard steps of using nonphysical values for the speed of light,  $c = 20v_A$ , and the electron-to-proton mass ratio,  $m_e/m_p = 1/25$ .

We enforce periodic boundary conditions in both the  $x$ - and  $y$ -directions and assume no variation in the  $z$ -direction. Velocities and fields have been calculated with three spatial components, but in a two-dimensional spatial domain with  $L_x = 102.4d_p$  and  $L_y = 25.6d_p$ . We use a grid spacing of  $\Delta x = 0.0125d_p$ , giving  $8192 \times 2048$  grid points in total, and use 50 particles per cell for the protons.

All simulations begin with a uniform magnetic field  $\mathbf{B} = B_0 \hat{x}$  and no electric field. Initial distribution functions for the protons and alphas consist of two populations of equal density: a cold ( $v_{th} < v_A$ ) Maxwellian background with  $T_c = 0.1m_p v_A^2$ , and a hot ( $v_{th} > v_A$ ) streaming population represented by an anisotropic, one-sided kappa function:

$$f_{\kappa} = \frac{\Gamma(\kappa + 1)}{\pi^{3/2} \theta_{\perp}^2 \theta_{\parallel} \kappa^{3/2} \Gamma(\kappa - 1/2)} \times \left[ 1 + \frac{v_x^2}{\kappa \theta_{\parallel}^2} + \frac{v_{\perp}^2}{\kappa \theta_{\perp}^2} \right]^{-(\kappa+1)} \Theta(v_x), \quad (2)$$

where  $\Gamma$  is the gamma function,  $\Theta$  is the Heaviside step function, and  $\theta_i^2 = (2T_i/m_i) * [(\kappa - 3/2)/\kappa]$ . For all simulations, we use  $\kappa = 2.5$  and an initial temperature anisotropy of  $T_{\kappa,x}/T_{\kappa,\perp} = 10$ .

This combined distribution models a population of accelerated ions that exhibits the nonthermal power-law tails often observed in flares (Reames et al. 1997; Mason 2007) and is streaming out

from a reconnection site into a cold background plasma. The equal density of the energetic population and cold ion background reflects the high efficiency of particle acceleration that is expected from reconnection (Arnold et al. 2021), while the large value of  $T_{\kappa,x}/T_{\kappa,\perp}$  is a consequence of Fermi reflection, which dominantly increases energy parallel to the ambient magnetic field (Drake et al. 2006; Dahlin et al. 2014).

We perform three runs with differing values of the initial energy of the streaming population: Run 1 has an initial  $T_{\kappa,x} = 10m_p v_A^2$ , while Run 2 is less energetic with an initial  $T_{\kappa,x} = 5m_p v_A^2$ , and Run 3 is more energetic with an initial  $T_{\kappa,x} = 20m_p v_A^2$ . For all runs, the initial distribution function of the electrons is a Maxwellian with  $T_e = 2m_p v_A^2$ . A small electron drift is also added to balance the current. The fully ionized  ${}^3\text{He}$  test particles are initialized as a Maxwellian with the same temperature as the cold ion background,  $T_c = 0.1m_p v_A^2$ .

## 4. Simulation Results

### 4.1. Waves Induced by the Initial Distribution Function

Simulations are run to a total time  $t = 150\Omega_{cp}^{-1}$ . Evolution of the proton and alpha temperature anisotropies, the combined proton and alpha parallel heat flux, and the out-of-plane magnetic field energy are presented in Figure 1. All three sets of initial conditions produce instabilities driven by both the temperature anisotropies and the parallel ion heat flux, with growth rates and peak perpendicular magnetic energies that increase as the initial energy of the streaming population is increased. Due to the complexity of the initial distribution functions, we have not analytically solved the linear dispersion

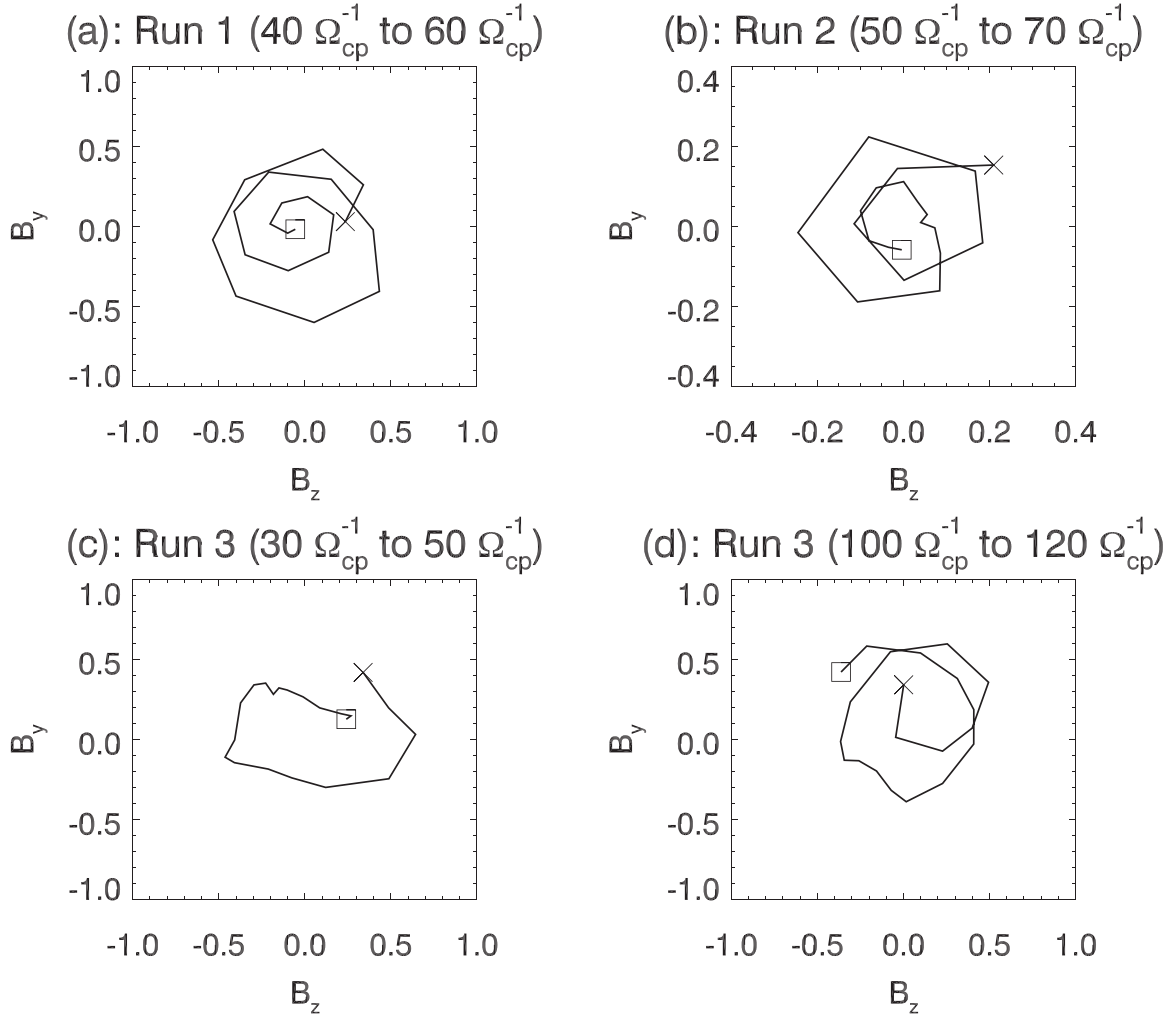


**Figure 2.** Hodograms ( $B_z$  vs.  $B_y$ ) at  $x = 25d_p$ ,  $y = 12.5d_p$ , every  $1 \Omega_{cp}^{-1}$  for each case. Initial times are indicated by the box, while final times are indicated by the X. The first three plots contain data around the peak of each instability: (a) 40–60  $\Omega_{cp}^{-1}$  for Run 1, (b) 50–70  $\Omega_{cp}^{-1}$  for Run 2, and (c) 30–50  $\Omega_{cp}^{-1}$  for Run 3. An additional plot with data near the end of Run 3 (100–120  $\Omega_{cp}^{-1}$ ) is included to show that the instability changes polarization at late time in the simulation.

relation. Therefore, we first analyze the characteristics of the waves measured in the simulations and then compare our results to the instabilities discussed in Section 2.

For Run 1, instability onset occurs around  $t = 35 \Omega_{cp}^{-1}$ . The wave amplitude peaks and stabilizes at  $t = 50 \Omega_{cp}^{-1}$ , with the perpendicular magnetic energy equal to around 10% that of the initial magnetic energy. By  $t = 60 \Omega_{cp}^{-1}$ , the anisotropies begin plateauing to their final values, while the heat flux continues to steadily decrease until  $t = 130 \Omega_{cp}^{-1}$ .

Decreasing the initial beam energy in Run 2 delays the time of instability onset, in this case occurring at  $t = 50 \Omega_{cp}^{-1}$ . Wave amplitude peaks and again stabilizes at  $t = 65 \Omega_{cp}^{-1}$ , with the perpendicular magnetic field energy equal to half that seen in Run 1. The final values of both anisotropies and the heat flux are higher than those of Run 1, as expected from the lower-energy fluctuations.

Increasing the initial beam energy in Run 3 leads to an instability which develops earlier in time, at  $t = 20 \Omega_{cp}^{-1}$ , and is significantly more energetic. Wave energy peaks at  $t = 45 \Omega_{cp}^{-1}$  with a perpendicular magnetic energy equal to nearly 30% of the initial magnetic energy. Unlike the two less energetic cases, some of this wave energy is then dissipated throughout the

simulation, ending with a final value equal to that of Run 1. There is a large reduction in both the heat flux and the anisotropies, with both the protons and alphas ending the run nearly isotropic in temperature.

With an understanding of the temporal evolution of the instabilities and drivers, we next look at the characteristics of the waves they produce. We calculate the wave polarizations for each run by plotting  $B_z$  versus  $B_y$  at a single point in the domain for 20 points in time spaced every  $1 \Omega_{cp}^{-1}$ . These results are presented in Figure 2. We then find the spectrum of unstable parallel ( $k_x$ ) and perpendicular ( $k_y$ ) wavenumbers by taking fast Fourier transforms (FFTs) of the out-of-plane magnetic field fluctuations over the whole domain. These results are presented in Figures 3–5. The phase velocities are calculated directly by comparing parallel and perpendicular cuts of the out-of-plane magnetic field data at multiple consecutive times. Finally, additional FFTs are taken spatially over the parallel direction and temporally over  $20 \Omega_{cp}^{-1}$  to produce the  $k_x$  versus  $\omega$  spectra presented in Figure 6. In order to reduce noise, each spectrum is averaged over the lower half of the spatial domain and calculated using the perpendicular magnetic field data multiplied by the function  $\sin^2(\pi(t - t_0)/T)$ , where  $t_0$  is the initial time and  $T$  is the total time period, ensuring periodicity in time.



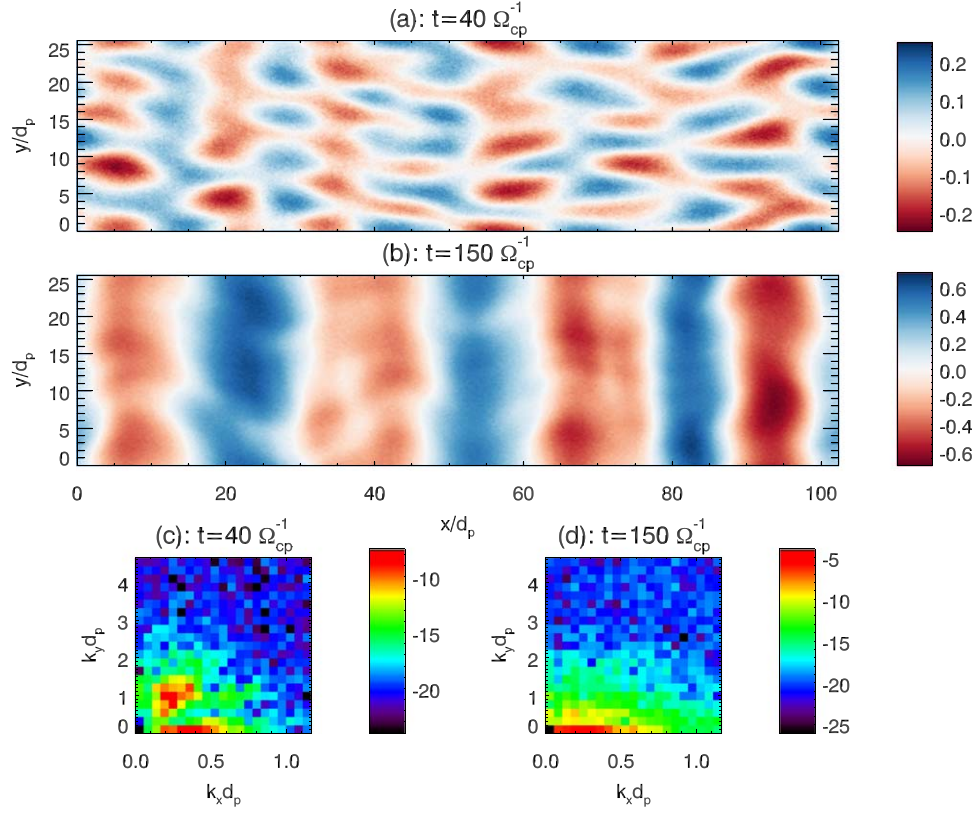


**Figure 3.** (a)–(b) Out-of-plane magnetic field data and (c)–(d) the natural logarithm of the FFT power spectra for Run 1 at early and late time. The spectra peak at  $k_y d_p = 0$  for both times, with  $k_x d_p = 0.37$  at  $t = 40 \Omega_{cp}^{-1}$  and  $k_x d_p = 0.18$  at  $t = 150 \Omega_{cp}^{-1}$ .

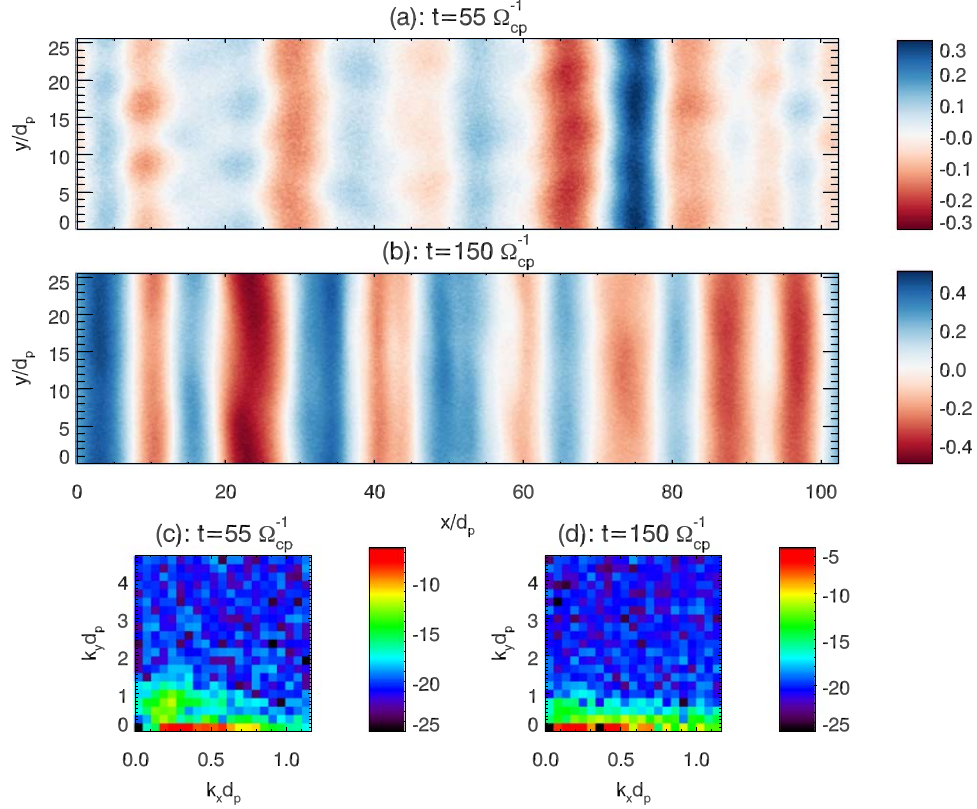


**Figure 4.** (a)–(b) Out-of-plane magnetic field data and (c)–(d) the natural logarithm of the spatial FFT power spectra for Run 2 at early and late time. The spectra peak at  $k_x d_p = 0.37$  and  $k_y d_p = 0$  for both times.

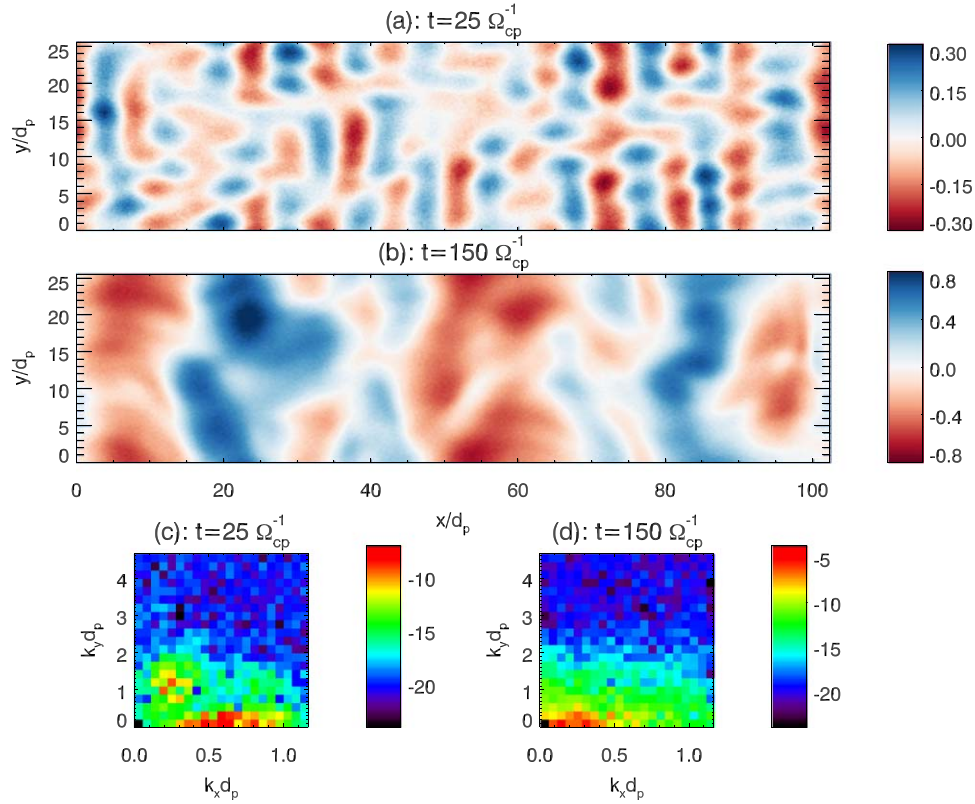


**Figure 5.** (a)–(b) Out-of-plane magnetic field data and (c)–(d) the natural logarithm of the spatial FFT power spectra for Run 3 at early and late time. The spectra peak at  $k_y d_p = 0$  for both times, with  $k_x d_p = 0.67$  at  $t = 25 \Omega_{cp}^{-1}$  and  $k_x d_p = 0.12$  at  $t = 150 \Omega_{cp}^{-1}$ .

The initial conditions of Run 1 excite right-hand polarized waves (Figure 2(a)). From the 2D plot of  $B_z$  in Figure 3(a) and the FFT in Figure 3(c), we see two modes at early time: a short-wavelength, perpendicular mode ( $k_y d_p \approx 1$ ,  $k_x \ll k_y$ ) and a longer-wavelength, parallel mode ( $k_x d_p < 1$ ,  $k_y \ll k_x$ ), both with a phase velocity  $v_p \approx 2v_A$  in the parallel direction. As time progresses, the perpendicular mode dissipates and by the end of the simulation we are left with predominantly parallel waves with increased wavelengths (see Figure 3(d)).

In the  $k_x$  versus  $\omega$  spectrum (Figure 6(a)), the majority of the wave power is in frequencies at and below the proton cyclotron frequency with corresponding parallel wavenumbers  $k_x d_p \leq 0.5$ , consistent with forward-propagating waves moving at  $2v_A$ . At higher wavenumbers and frequencies, the power from this mode decreases before dropping off around  $k_x d_p = 1$  and  $\omega = 2\Omega_{cp}$ . Two additional weak modes exist above  $k_x d_p = 1$ , with both positive and negative frequencies greater than  $\Omega_{cp}$ , corresponding to forward- and backward-propagating modes.

In the less energetic Run 2, the perpendicular mode is significantly weaker and dissipates much quicker than in Run 1, thus the instability has very little perpendicular structure throughout the simulation (Figures 4(a) and (c)). In addition, this case has higher wavenumbers at late time (Figures 4(b) and (d)) and the backward-propagating mode that appears in the  $k_x$  versus  $\omega$  spectrum is weaker (Figure 6(b)). Apart from this, the characteristics remain similar to those seen in Run 1: the waves are right-hand polarized (Figure 2(b)), with a parallel phase speed  $v_p \approx 2v_A$ , frequencies up to the proton cyclotron frequency, and small wavenumbers ( $k_x d_p < 1$ ).

Raising the initial energy in Run 3 once again produces a short-wavelength, perpendicular mode with wavenumbers similar to those seen in Run 1 (Figures 5(a) and (c)). However,

the parallel mode at early time is significantly different, with larger wavenumbers, a left-handed polarization (Figure 2(c)), and a much slower phase speed ( $v_p < v_A$ ), corresponding to lower frequencies:  $\omega < 0.5 \Omega_{cp}$  (Figure 6(c)). Apart from this, the  $k_x$  versus  $\omega$  spectrum at early time is similar to those of the previous two cases, albeit more diffuse due to the changing wavenumbers during this period.

Later in the run, the perpendicular mode weakens and the parallel mode begins to resemble those of the other two cases: The polarization becomes right-handed (Figure 2(d)) and the wavenumbers decrease (Figure 5(d)), while the frequency remains roughly constant (Figure 6(d)), leading to an increase in the phase velocity. The higher-frequency modes also disappear at this time, leaving only the primary mode with peak frequencies below the proton cyclotron frequency and  $k d_p < 0.5$ .

While our initial distribution functions are far from the simple Maxwellians considered in the literature (see discussion in Section 2), it may still be useful to compare our results to the linear instabilities previously discussed. To do this, we shift to the rest frame of the full proton and alpha distributions. This corresponds to a frame moving parallel to the magnetic field at  $\approx 1v_A$  for Run 1,  $\approx 0.75v_A$  for Run 2, and  $\approx 1.5v_A$  for Run 3. In this frame, the parallel mode in Run 1, Run 2, and at late time in Run 3 is a forward-propagating right-handed wave with a phase speed  $v_p \approx v_A$  and frequencies around  $0.3\Omega_{cp}$ . It is most likely a form of the right-hand resonant instability or possibly a combination of the right-hand resonant and parallel fire-hose instabilities. At early time in Run 3, this mode has similar characteristics, but is backward propagating, unlike any of the instabilities discussed in Section 2.

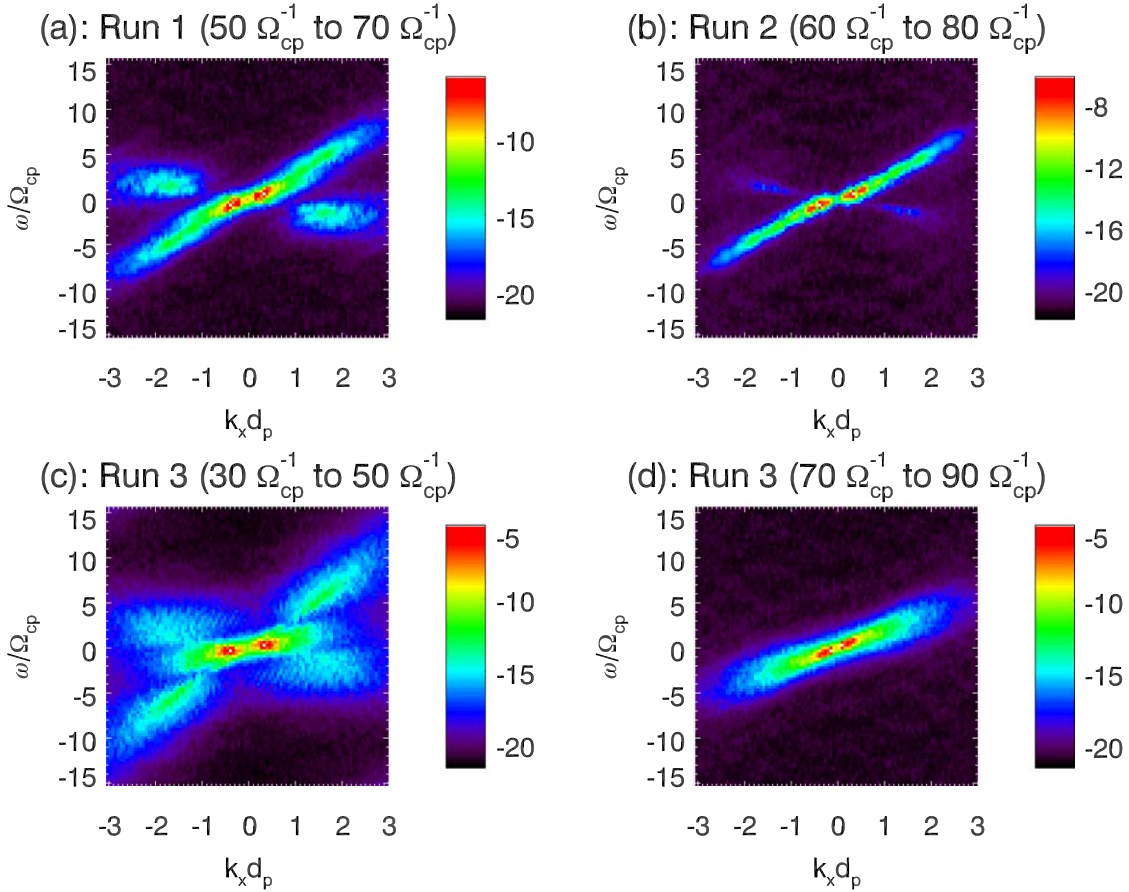


**Figure 6.** The natural logarithm of the power spectra for FFTs along the parallel direction in space and over  $20 \Omega_{cp}^{-1}$  in time for (a) Run 1 at  $t = 50\text{--}70 \Omega_{cp}^{-1}$ , (b) Run 2 at  $t = 60\text{--}80 \Omega_{cp}^{-1}$ , (c) Run 3 at  $t = 30\text{--}50 \Omega_{cp}^{-1}$ , and (d) Run 3 at  $t = 70\text{--}90 \Omega_{cp}^{-1}$ . Each plot is the average of 1024 FFTs taken along each horizontal cut in the lower half of the domain. Peaks occur at (a)  $k_x d_p = 0.37$ ,  $\omega/\Omega_{cp} = 0.63$ , (b)  $k_x d_p = 0.37$ ,  $\omega/\Omega_{cp} = 0.63$ , (c)  $k_x d_p = 0.37$ ,  $\omega/\Omega_{cp} = 0.31$ , and (d)  $k_x d_p = 0.12$ ,  $\omega/\Omega_{cp} = 0.31$ .

The oblique mode appears to have an energy threshold for instability, as it only appears in the higher-energy cases of Runs 1 and 3, though it is unclear how it relates to the linear instabilities previously discussed. Likewise, we have not identified the high-frequency modes that appear in the  $k_x$  versus  $\omega$  spectra; however, given that they are considerably weaker than the dominant mode and do not appear in the  $k_x$  versus  $k_y$  spectra, it is not likely that they play a significant role in the simulation dynamics.

#### 4.2. Proton and Alpha Wave-Particle Interactions

To study the wave-particle interactions driving these instabilities, we generate velocity distribution functions for the protons and the alphas every  $10 \Omega_{cp}^{-1}$ . Because  $B_x$  remains the dominant magnetic field component for the duration of each simulation, the velocities  $v_y$  and  $v_z$  remain the dominant perpendicular components, with  $v_x$  the parallel component. For simplicity, we display the  $v_x$ – $v_y$  velocity distribution functions to illustrate the relaxation of the initial anisotropic distribution functions as the instabilities develop. Proton distributions from the beginning, middle, and end of each run are presented in Figure 7. The dynamics of the alpha particles are similar to those of the protons in all cases and therefore are not shown here.

In Run 2, where there are no oblique modes, wave-particle interactions occur only at the  $n = +1$  resonance or  $v_{||} = (\omega + \Omega_{cp})/k_{||} = 2v_A + \Omega_{cp}/k_{||}$ . Particles from the high-energy tail

of the distribution scatter along circular orbits centered at  $v_x = 2v_A$ , corresponding to constant-energy surfaces in the frame of the wave. The lower-energy particles scatter first and contribute to the growth of the instability. As time progresses and the parallel wavenumbers decrease, the higher-energy particles become resonant. However, due to the fewer number of particles at high energies, the total energy transferred to the waves by these particles is relatively low. Without multiple resonances, particle scattering in this case is limited and there remains a clear drop-off in the distributions around  $v_x = 0$ . This is consistent with the quasi-linear theory for parallel waves, wherein particles are unable to scatter past  $90^\circ$  in pitch angle.

In Runs 1 and 3, where there are finite-amplitude oblique modes, a variety of resonances ( $n = 0, \pm 1, \pm 2$ , and  $\pm 3$ ) overlap and efficiently scatter particles from positive to negative parallel velocities. An example of this is given in Figure 8, where we have calculated the resonance widths for Run 1 using Equations (5)(a)–(g) from Karimabadi et al. (1992), assuming circularly polarized waves with positive helicity ( $A_1 = A_2 = \delta B/k_{||}$ ) and no electrostatic component ( $\Phi_0 = 0$ ). As in the parallel case, particles in Run 1 scatter along circles centered at  $v_x = 2v_A$ . In Run 3, the dynamics are much more chaotic due to the changing phase speed of the waves. In both cases, it is once again the lower-energy particles that scatter first and contribute the most energy toward wave growth. Along with the broad range of wavenumbers in both cases, resonance overlap allows the majority of velocity space to diffuse in pitch angle, and particles are able to scatter into near-isotropic distributions by the end of



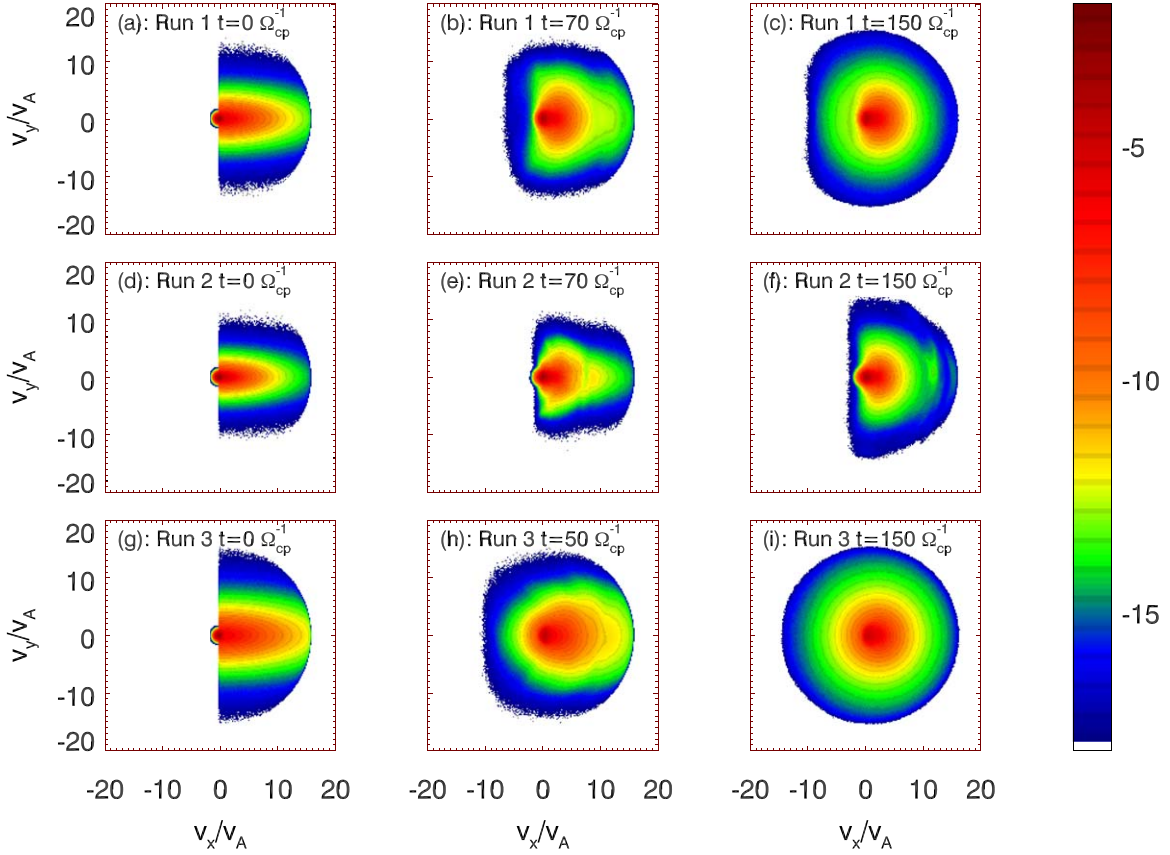


**Figure 7.** Velocity distribution functions for the protons at the beginning, middle, and end of Run 1 (a)–(c), Run 2 (d)–(f), and Run 3 (g)–(i). Each distribution is plotted on the same logarithmic scale and is normalized to 1.

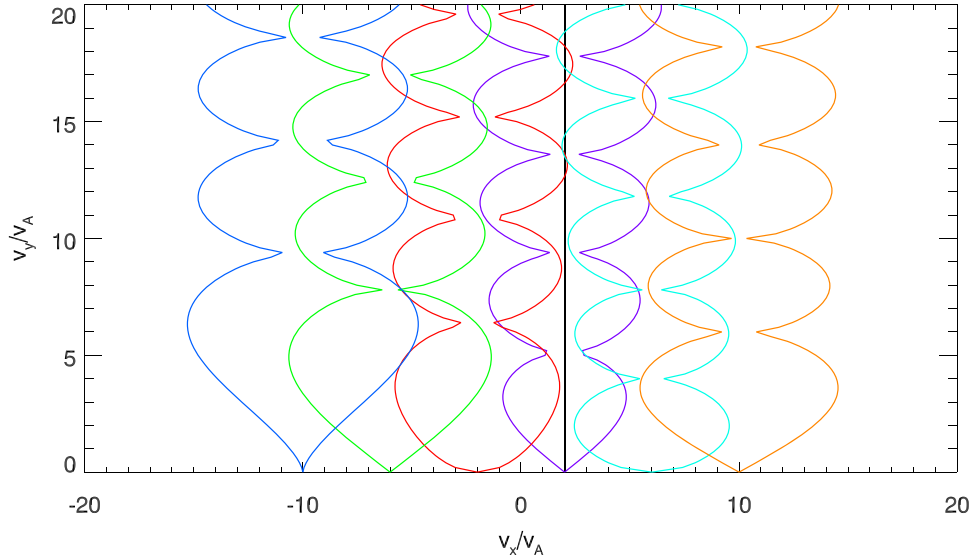


**Figure 8.** Proton resonance widths at  $t = 70 \Omega_{cp}^{-1}$  for Run 1, using  $k_{\parallel} = 0.25d_p$  and  $k_{\perp} = 0.75d_p$ . The phase speed of the wave is plotted in black, while the  $n = -3$  (blue),  $n = -2$  (green),  $n = -1$  (red),  $n = 0$  (purple),  $n = 1$  (cyan), and  $n = 2$  (orange) resonances are plotted as the area enclosed by each curve. Wavenumbers were selected by taking the strongest oblique mode from the FFT power spectrum, and the fluctuation amplitude used is the rms average over the box.

the simulations. This is most apparent in the final distributions for Run 3.

#### 4.3. $^3\text{He}$ Resonance Heating

The  $^3\text{He}$  dynamics have been calculated in all three cases; however, as previously stated in Section 3, we neglect the

feedback of these particles on the simulation because of their low density in the corona. In the same manner as the protons and alphas, we generate velocity distribution functions for the  $^3\text{He}$  ions every  $10\Omega_{cp}^{-1}$ . Three times from each case are presented in Figure 9. We also calculate the parallel and perpendicular temperatures of the  $^3\text{He}$  directly from the full, three-dimensional distribution functions. The



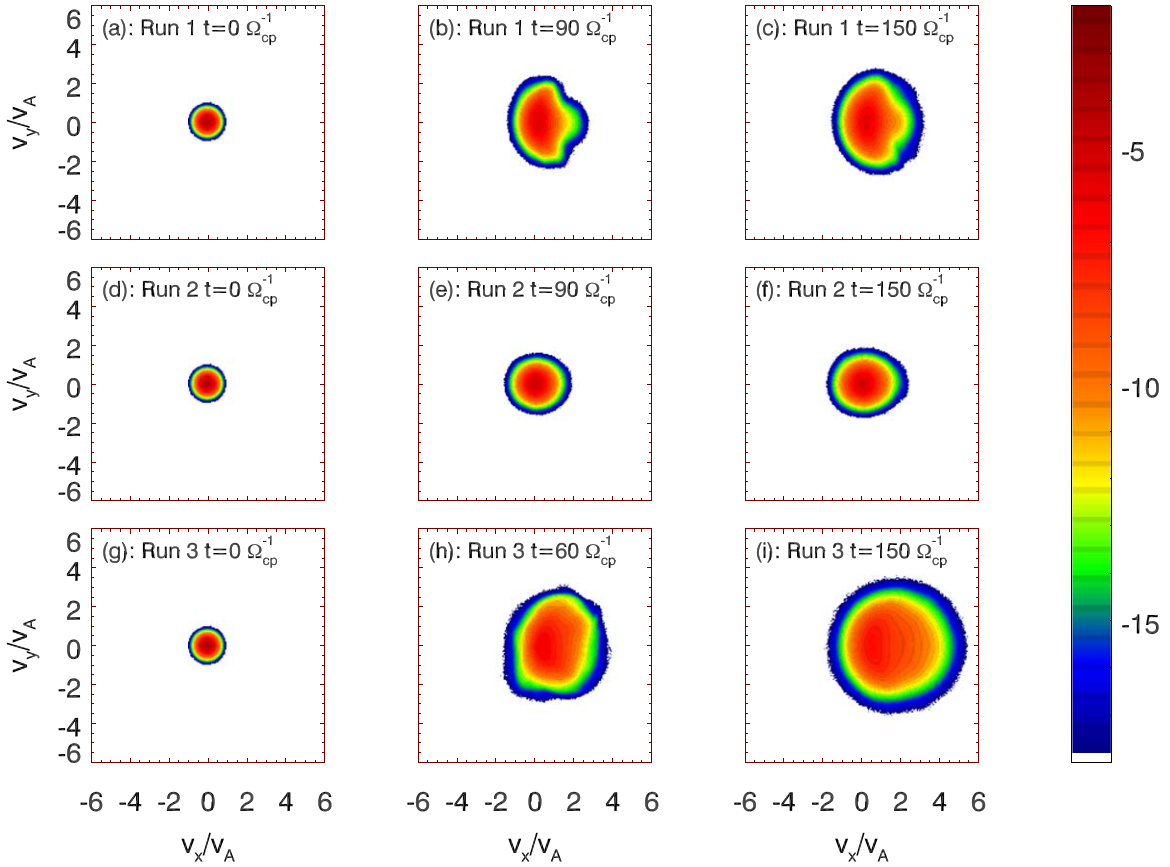


**Figure 9.** Velocity distribution functions of the  $^3\text{He}$  test particles at the beginning, middle, and end of (a)–(c) Run 1, (d)–(f) Run 2, and (g)–(i) Run 3. Each distribution is plotted on the same logarithmic scale and is normalized to 1.

temperatures versus time for all three runs are presented in Figure 10.

In all cases, the resonant velocity at  $v_{\parallel} = (\omega + \Omega_{\text{cp}})/k_{\parallel}$  is much greater than the initial thermal velocity of the  $^3\text{He}$ , and thus this resonance does not contribute to the initial heating of these particles. For Run 2, where this is the only active resonance, this means that the  $^3\text{He}$  heating throughout the run is minimal in both the parallel and perpendicular directions.

For Run 1, where there are oblique waves at early time,  $^3\text{He}$  is initially heated in the perpendicular direction by the  $n = -1$  resonance and in the parallel direction by the  $n = 0$  resonance. This is most clearly demonstrated in Figure 9(b), where positive-velocity particles are pulled toward the phase speed of the wave,  $v_p = 2v_A$ , while negative-velocity particles are pulled upwards and into circular orbits about  $v_p$ . As time progresses, particles that have been heated in the perpendicular direction also gain parallel energy due to resonance broadening and overlap of the  $n = -1$ , 0, and  $+1$  resonances (Figure 11), though the majority of the energy gained remains in the perpendicular direction.

The heating and scattering of  $^3\text{He}$  is most effective in Run 3 due to the changing phase speed and polarization of the waves. At early time, the waves are left-hand polarized and strong perpendicular heating initially occurs through the primary ( $n = +1$ ) resonance at  $v_{\parallel} = (\omega - \Omega_{\text{cp}})/k_{\parallel}$ . As the phase speed of the wave changes, the particle orbits no longer follow the simple concentric circles discussed in Section 2 and instead become chaotic, leading to more isotropic heating, as reflected in Figure 9(h). Once the polarization of the waves switches and the primary resonance moves to  $v_{\parallel} = (\omega + \Omega_{\text{cp}})/k_{\parallel}$ , additional

scattering and parallel heating also occurs, allowing the final distribution to more closely resemble a Maxwellian than in the previous two cases.

## 5. Discussion and Conclusions

We have shown, using fully kinetic plasma simulations, that energetic protons and alpha particles streaming into a region of colder plasma can generate ion-scale instabilities ( $kd_p \lesssim 1$ ). For sufficiently large energies, both parallel and oblique modes are excited, leading to resonances at both positive and negative velocities. Resonance overlap occurs as the fluctuation amplitudes increase, allowing the energetic particles to scatter out of the tails of the distributions, past  $90^\circ$  in pitch angle and into negative velocities. For the most energetic initial conditions, this scattering is very efficient and results in nearly isotropic distributions by the end of the simulation. The scattering time is around  $100 \Omega_{\text{cp}}^{-1}$ , corresponding to  $\approx 10^{-2}$  s in the corona. For the highest-energy ions, this gives a mean free path of  $\approx 1$  Mm, within the typical size (tens of megameters) of the flare energy release region. Therefore, we expect that ions with large parallel energies due to reconnection will generate finite-amplitude waves that act to scatter parallel energy into perpendicular energy and therefore inhibit energetic ion transport out of the flare energy release region.

These waves are also effective at heating trace amounts of  $^3\text{He}$ , increasing both the parallel and perpendicular temperatures by a factor of nearly 20 in the most energetic of our simulations. A key question, however, is whether these waves are capable of boosting the abundance of  $^3\text{He}$  in impulsive

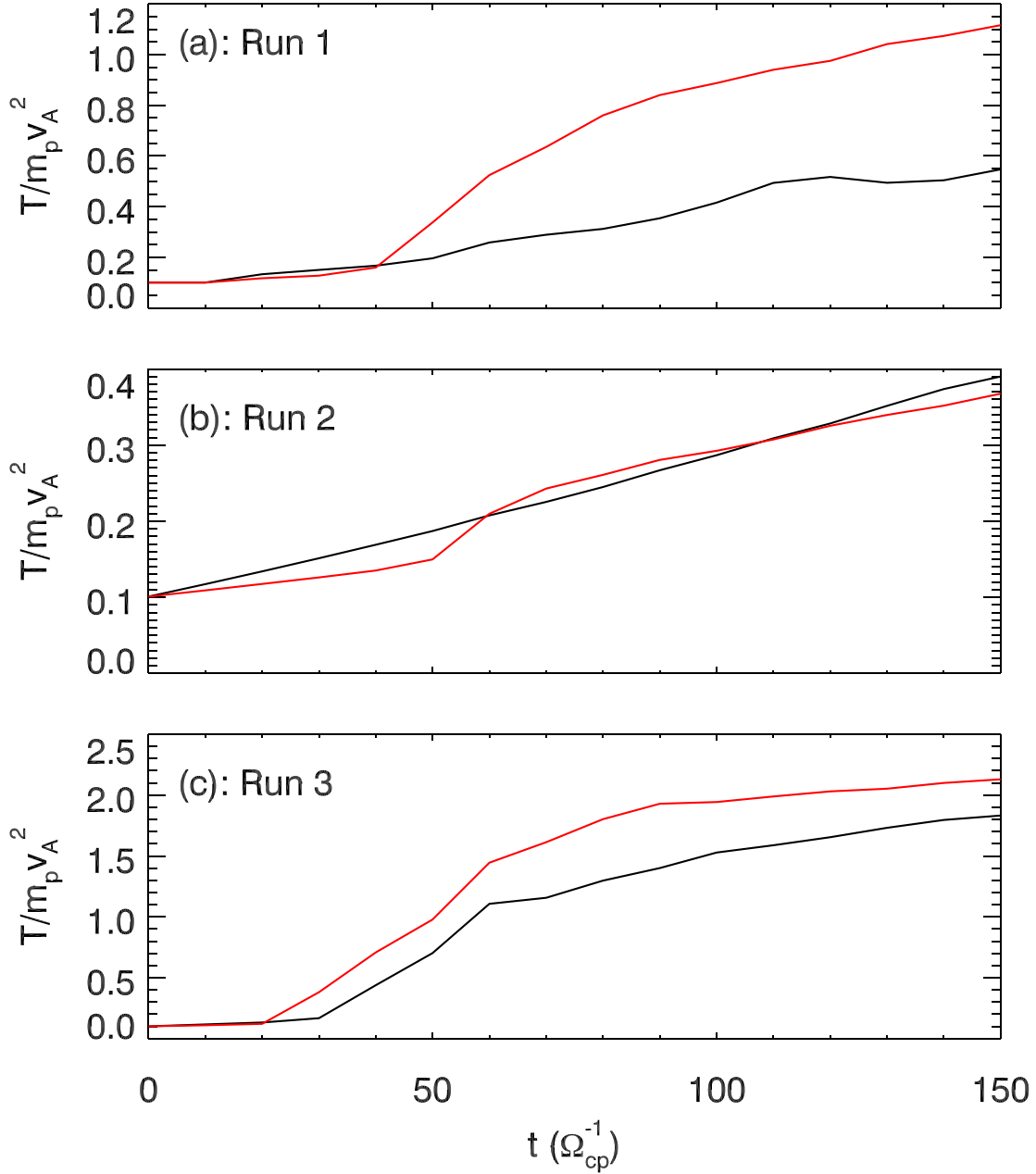


**Figure 10.** Parallel (black) and perpendicular (red)  ${}^3\text{He}$  temperatures vs. time for each run, with data plotted every  $10 \Omega_{\text{cp}}^{-1}$ . Note that the vertical scale changes between each plot.

flares. In the model by Temerin & Roth (1992), left-handed waves driven by electron beams at or slightly below the proton cyclotron frequency propagate into regions of higher magnetic field. As these waves propagate, their frequency remains constant, while the ion cyclotron frequencies increase proportional to the increasing field. The  ${}^3\text{He}$  resonance condition for these waves is given by  $v_{\parallel} = (\omega - \Omega_{\text{ci}})/k_{\parallel}$ , where  $\Omega_{\text{ci}} = (2/3)\Omega_{\text{cp}}$  is the  ${}^3\text{He}$  cyclotron frequency. Because the ambient  ${}^3\text{He}$  outside of the flare energy release region is cold, the resonance interaction requires  $\omega \sim \Omega_{\text{ci}}$ . Since  ${}^3\text{He}$  has the highest cyclotron frequency of all of the nonprotons in the corona, it will be the first ion species to resonate with these waves and can be preferentially accelerated during a flare.

As we have shown, however, ion beams that are produced during flare energy release are efficient drivers of oblique right- and left-handed waves in the range of the proton cyclotron

frequency and below (see Figure 12). Thus, similar arguments suggest that the waves on the higher end of this frequency spectrum should drive  ${}^3\text{He}$  abundance enhancements, with waves in the frequency range  $0.5\Omega_{\text{cp}} < \omega < 0.67\Omega_{\text{cp}}$  affecting particle populations above the flare site and waves in the frequency range  $0.67\Omega_{\text{cp}} < \omega < \Omega_{\text{cp}}$  affecting particle populations below the flare site. However, because these waves are oblique, both right- and left-handed waves can resonate with cold  ${}^3\text{He}$ . In the case of left-handed waves, it is the  $n = +1$  resonance in Equation (1), while for right-handed waves it is the  $n = -1$  resonance that will heat cold  ${}^3\text{He}$ . The heated particles will then stream into the flare energy release region, where they will be further accelerated to observed energies by Fermi reflection during reconnection (Drake et al. 2006, 2012).

In our simulations, the  ${}^3\text{He}$  is heated to a thermal speed  $\sim v_A$  (see Figures 9 and 10). Thus, the total energy flux of the heated

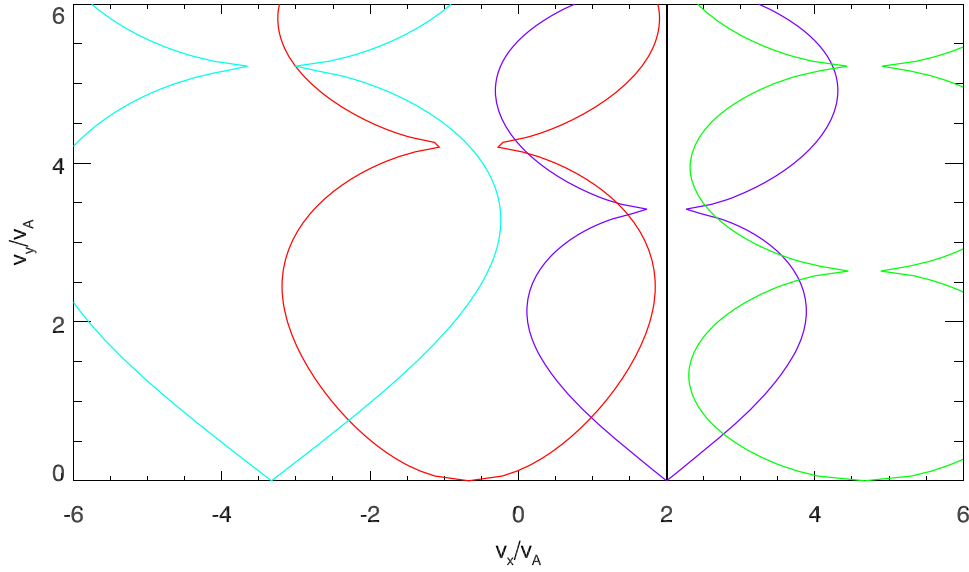


**Figure 11.**  $^3\text{He}$  resonance widths at  $t = 50 \Omega_{\text{cp}}^{-1}$  for Run 1, using  $k_{\parallel} = 0.25d_p$  and  $k_{\perp} = 0.75d_p$ . The phase speed of the wave is plotted in black, while the  $n = -2$  (cyan),  $n = -1$  (red),  $n = 0$  (purple), and  $n = 1$  (green) resonances are plotted as the area enclosed by each curve. Wavenumbers were selected by taking the strongest oblique mode from the FFT power spectrum, and the fluctuation amplitude used is the rms average over the box.

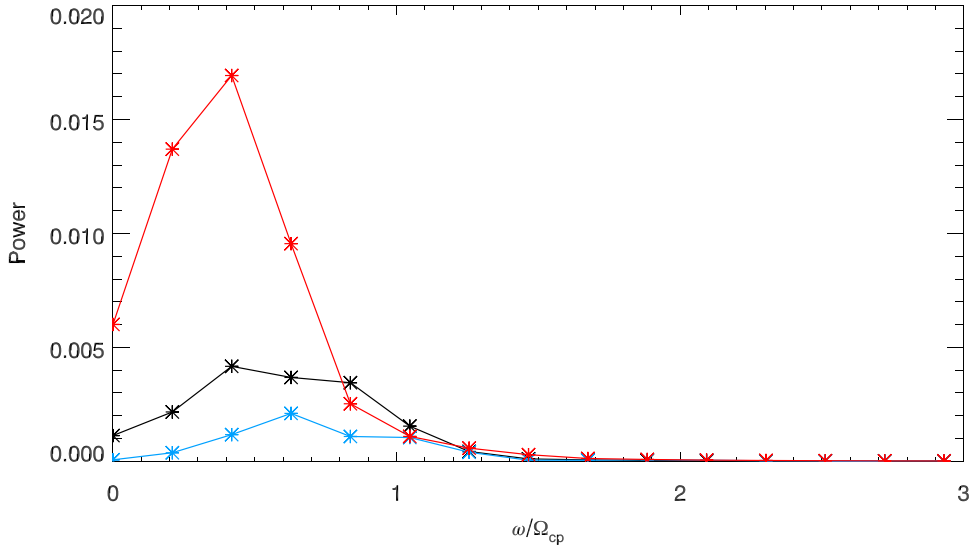


**Figure 12.** The temporal FFT power spectrum at low frequencies for Run 1 at  $t = 50\text{--}80 \Omega_{\text{cp}}^{-1}$  (black), Run 2 at  $t = 60\text{--}90 \Omega_{\text{cp}}^{-1}$  (blue), and Run 3 at  $t = 40\text{--}70 \Omega_{\text{cp}}^{-1}$  (red). FFTs were calculated in the same way as Figure 6 and then summed over  $k_x$ .

particles moving into the flare region will be  $(1/4)n_{3\text{He}}m_{3\text{He}}v_A^3$ , with an additional factor of  $1/2$  accounting for some particle transport in the opposite direction. The electromagnetic energy of the waves responsible for heating is  $\tilde{B}^2/8\pi$ , where  $\tilde{B}$  is the average magnetic field amplitude of waves with frequencies  $0.5\Omega_{\text{cp}} \leq \omega \leq \Omega_{\text{cp}}$ . Like Alfvén waves, the plasma energy of cyclotron waves is roughly equal to the field energy. Using  $2v_A$  as the wave velocity, this gives a wave energy flux equal to  $\tilde{B}^2 v_A/2\pi$ . Equating this with the  $^3\text{He}$  energy flux and neglecting factors of order unity, we find that the number density of heated  $^3\text{He}$  is directly proportional to the squared amplitude of the wave magnetic field:  $n_{3\text{He}}/n_p \sim \tilde{B}^2/B_0^2$ , where  $n_p$  is the number density of the protons and  $B_0$  is the background magnetic field. We emphasize that  $\tilde{B}$  in this expression only corresponds to the wave energy in the frequency band  $0.5\Omega_{\text{cp}} \leq \omega \leq \Omega_{\text{cp}}$ .

Using the FFT frequency spectra, we can obtain  $\tilde{B}^2$  by calculating the fraction of power in the frequency range  $0.5\Omega_{\text{cp}} \leq \omega \leq \Omega_{\text{cp}}$ . To do this, we fit the data presented in Figure 12 from  $\omega = 0$  to  $\omega = 1.5\Omega_{\text{cp}}$  with polynomials. We then calculate the fraction of the energy in the range  $0.5\Omega_{\text{cp}} \leq \omega \leq \Omega_{\text{cp}}$  using the polynomial representation. Excluding the lowest-energy case, which did not produce good  $^3\text{He}$  heating, these fractions are 46% for Run 1 and 31% for Run 3. From Figure 1(d), the average value of  $B_z^2/B_0^2$  over the time period of the FFTs is 8.5% for Run 1 and 22% for Run 3; therefore,  $\tilde{B}^2/B_0^2$  is 3.91% for Run 1 and 6.82% for Run 3. These percentages are on the order of the  $^4\text{He}$  density in the corona. We emphasize, of course, that in our picture of  $^3\text{He}$  abundance enhancement the waves are responsible for driving  $^3\text{He}$  into the flare site and raising their energy to the range of  $m_{3\text{He}}v_A^2 \sim 10 \text{ keV nucleon}^{-1}$ , but it is reconnection-

driven energization that further accelerates these particles to energies of the order of  $0.1\text{--}10\text{ MeV nucleon}^{-1}$  (Mason 2007).

Thus, energetic ion beams are a strong candidate for driving the waves responsible for the enhancements of  $^3\text{He}$  observed in impulsive flares. However, further simulations are needed to explore how the  $^3\text{He}$  is resonantly heated in an inhomogeneous magnetic field. In addition, a numerical analysis of the dispersion relation using Equation (2) should be able to establish definitively the instabilities responsible for the waves observed in our simulations. Ongoing work in this area using the Arbitrary Linear Dispersion Solver (Verscharen et al. 2018) will be covered in a future paper.

### Acknowledgments

The authors were supported by NSF grant No. PHY2109083 and NASA grant Nos. 80NSSC20K1813 and 80NSSC23K1625. This study benefits from discussions within the International Space Science Institute (ISSI) Team ID 425 “Origins of 3He-rich SEPs.” We acknowledge informative discussions with Drs. R. Bucik and G. Mason. The PIC simulations were performed at the National Energy Research Supercomputing Center.

### ORCID iDs

J. F. Drake  <https://orcid.org/0000-0002-9150-1841>

M. Swisdak  <https://orcid.org/0000-0002-5435-3544>

### References

- Arnold, H., Drake, J. F., Swisdak, M., et al. 2021, *PhRvL*, **126**, 135101
- Bučík, R. 2020, *SSRv*, **216**, 24
- Dahlin, J. T., Drake, J. F., & Swisdak, M. 2014, *PhPl*, **21**, 092304
- Drake, J. F., Swisdak, M., Che, H., & Shay, M. A. 2006, *Natur*, **443**, 553
- Drake, J. F., Swisdak, M., & Fermo, R. 2012, *ApJL*, **763**, L5
- Eastwood, J. P., Phan, T. D., Drake, J. F., et al. 2013, *PhRvL*, **110**, 225001
- Fisk, L. A. 1978, *ApJ*, **224**, 1048
- Gabriel, A. H., Culhane, J. L., Patchett, B. E., et al. 1995, *AdSpR*, **15**, 63
- Gary, S. P. 1985, *ApJ*, **288**, 342
- Gary, S. P. 1991, *SSRv*, **56**, 373
- Gary, S. P. 1993, *Theory of Space Plasma Microinstabilities* (Cambridge: Cambridge Univ. Press)
- Gary, S. P., Montgomery, M., Feldman, W., & Forslund, D. 1976, *JGR*, **81**, 1241
- Gary, S. P., Smith, C. W., Lee, M. A., Goldstein, M. L., & Forslund, D. W. 1984, *PhFl*, **27**, 1852
- Hellinger, P., & Matsumoto, H. 2000, *JGR*, **105**, 10519
- Karimabadi, H., Akimoto, K., Omid, N., & Menyuk, C. R. 1990, *PhFIB*, **2**, 606
- Karimabadi, H., Krauss-Varban, D., & Terasawa, T. 1992, *JGR*, **97**, 13853
- Kennel, C. F., & Engelmann, F. 1966, *PhFl*, **9**, 2377
- Kennel, C. F., & Petschek, H. E. 1966, *JGR*, **71**, 1
- Lin, R. P. 2011, *SSRv*, **159**, 421
- Mason, G. M. 2007, *SSRv*, **130**, 231
- Mason, G. M., Roth, I., Nitta, N. V., et al. 2023, *ApJ*, **957**, 112
- Moses, J. D., Antonucci, E., Newmark, J., et al. 2020, *NatAs*, **4**, 1134
- Paesold, G., Kallenbach, R., & Benz, A. O. 2003, *ApJ*, **582**, 495
- Reames, D. V. 1999, *SSRv*, **90**, 413
- Reames, D. V. 2021, *Solar Energetic Particles: A Modern Primer on Understanding Sources, Acceleration and Propagation* (Berlin: Springer)
- Reames, D. V., Barbier, L. M., Von Rosenvinge, T. T., et al. 1997, *ApJ*, **483**, 515
- Roth, I., & Temerin, M. 1997, *ApJ*, **477**, 940
- Shih, A. Y., Lin, R. P., & Smith, D. M. 2009, *ApJL*, **698**, L152
- Temerin, M., & Lysak, R. L. 1984, *JGR*, **89**, 2849
- Temerin, M., & Roth, I. 1992, *ApJL*, **391**, L105
- Verniero, J. L., Larson, D. E., Livi, R., et al. 2020, *ApJS*, **248**, 5
- Verscharen, D., Klein, K. G., Chandran, B. D. G., et al. 2018, *JPIPh*, **84**, 905840403
- Wilson, L. B., III 2016, *Low-Frequency Waves in Space Plasmas* (Washington, DC: American Geophysical Union), 269
- Winske, D., & Leroy, M. M. 1984, *JGR*, **89**, 2673
- Zeiler, A., Biskamp, D., Drake, J. F., et al. 2002, *JGRA*, **107**, 1230
- Zhang, T. X. 1999, *ApJ*, **518**, 954